n-Type thermoelectric elastomers

https://doi.org/10.1038/s41586-025-09387-z

Received: 2 April 2024

Accepted: 10 July 2025

Published online: 13 August 2025

Check for updates

Kai Liu[1,6], Jingyi Wang[1,6], Xiran Pan[1], Shuang-Yan Tian[1], Yudong Liu[2], Zhi Zhang[1], Yuqiu Di[3,4], Jupeng Chen[1], Chengwen Wu[1], Xin-Yu Deng[1], Dongyang Wang[3,4], Peiyun Li[1], Chen-Kai Pan[5], Fenglian Qi[2], Jinhui Liu[2], Jing Hua[2], Jian Pei[5], Chong-an Di[3,4], Yunlong Guo[3,4], Yunqi Liu[3,4] & Ting Lei[1]✉

Intrinsically elastic thermoelectric generators with superior conformal coverage and shape adaptability are highly desirable for developing self-powered wearable electronics, soft bioelectronics and personal temperature regulators[1,2]. Until now, all reported high-performance thermoelectric materials have realized only flexibility, rather than elasticity[3,4]. Here we present one of the first n-type thermoelectric elastomers by integrating uniform bulk nanophase separation, thermally activated crosslinking and targeted doping into a single material. The thermoelectric elastomers could exhibit exceptional rubber-like recovery of up to 150% strains and high figure of merit values rivalling flexible inorganic materials even under mechanical deformations. Conventional wisdom suggests that incorporating insulating polymers should dilute the active component in organic thermoelectrics, resulting in lower performance. However, we demonstrate that carefully selected elastomers and dopants can promote the formation of uniformly distributed, elastomer-wrapped and heavily n-doped semiconducting polymer nanofibrils, leading to improved electrical conductivity and decreased thermal conductivity. These thermoelectric elastomers have the potential to make elastic thermoelectric generators in wearable applications much more conformable and efficient.

Thermoelectric conversion is a sustainable energy harvesting technology that can directly convert temperature gradients into voltage and vice versa[5–7]. Driven by the growing demand for wearable electronics and soft bioelectronics, thermoelectric generators (TEGs) that are soft, elastic and behave like skin are ideally suited as power sources for these electronics[8,9]. Compared with thermionic capacitors and thermocells, thermoelectrics are a promising candidate for low-grade heat harvesting because of their low internal resistances and high power densities[7]. Skin-like TEGs, characterized by low elastic modulus and high tensile deformability, must possess structural freedom to ensure sufficient thermal contact with three-dimensional (3D) complex-shaped objects or the human body to improve heat collection efficiency while maintaining good comfort and shape adaptability[1,10]. Despite marked advances in enhancing thermoelectric conversion efficiency, the existing TEGs are seldom capable of accommodating repetitive mechanical deformations, such as those associated with human movements, which typically necessitate strains of 5–50% (refs. 8,11).

Thermoelectric performance is assessed using a dimensionless figure of merit, $ZT = \sigma S^2 T/\kappa$, where σ denotes the electrical conductivity, S the Seebeck coefficient and κ the thermal conductivity[12]. Pioneering research has focused on enhancing the mechanical flexibility of thermoelectric materials, an important requirement for viable wearable applications. Materials based on inorganic bismuth telluride have increased room-temperature thermoelectric performance and excellent flexibility, having been widely used in flexible TEG fabrication[13,14]. Recently, inherently ductile inorganic thermoelectric materials, such as $(AgCu)_{0.998}Se_{0.22}S_{0.08}Te_{0.7}$, have been developed. These materials have impressive ZT values reaching 0.45 at 300 K (ref. 3). By contrast, although doped semiconducting polymers offer advantages, including low thermal conductivity, good mechanical flexibility, low toxicity and large-area solution processability, their thermoelectric performance remains limited[15,16].

Elastic electronics based on semiconducting polymers have generated a lot of research interest because of their potential in on-skin sensors and implantable bioelectronics[17]. So far, elastic conductors[18], light-emitting diodes[19] and transistors[20] have been developed. Previous studies have explored the development of stretchable p-type thermoelectric polymers through approaches such as molecular design or elastomer blending[21,22]. Nonetheless, these materials exhibit low power factor (PF) values and insufficient elasticity, making them unsuitable for practical TEG applications. Moreover, fabricating stretchable or elastic n-type thermoelectric materials presents a more formidable challenge, primarily due to substantial energetic disorder and poor stability caused by the weak reducing abilities and large sizes of n-dopants[15,23,24].

Here we report one of the first n-type thermoelectric elastomers (TEEs) created through uniform bulk nanophase separation, thermally activated crosslinking and targeted doping. These TEEs exhibit

[1]National Key Laboratory of Advanced Micro and Nano Manufacture Technology, Key Laboratory of Polymer Chemistry and Physics of Ministry of Education, School of Materials Science and Engineering, Peking University, Beijing, China. [2]Key Laboratory of Rubber-Plastics, Ministry of Education/Shandong Provincial Key Laboratory of Rubber-plastics, Qingdao University of Science and Technology, Qingdao, China. [3]Beijing National Laboratory for Molecular Sciences, Key Laboratory of Organic Solids, Institute of Chemistry Chinese Academy of Sciences, Beijing, China. [4]School of Chemistry and Chemical Engineering, University of Chinese Academy of Sciences, Beijing, China. [5]Beijing National Laboratory for Molecular Sciences (BNLMS), Key Laboratory of Polymer Chemistry and Physics of Ministry of Education, Center of Soft Matter Science and Engineering, College of Chemistry and Molecular Engineering, Peking University, Beijing, China. [6]These authors contributed equally: Kai Liu, Jingyi Wang. ✉e-mail: tinglei@pku.edu.cn

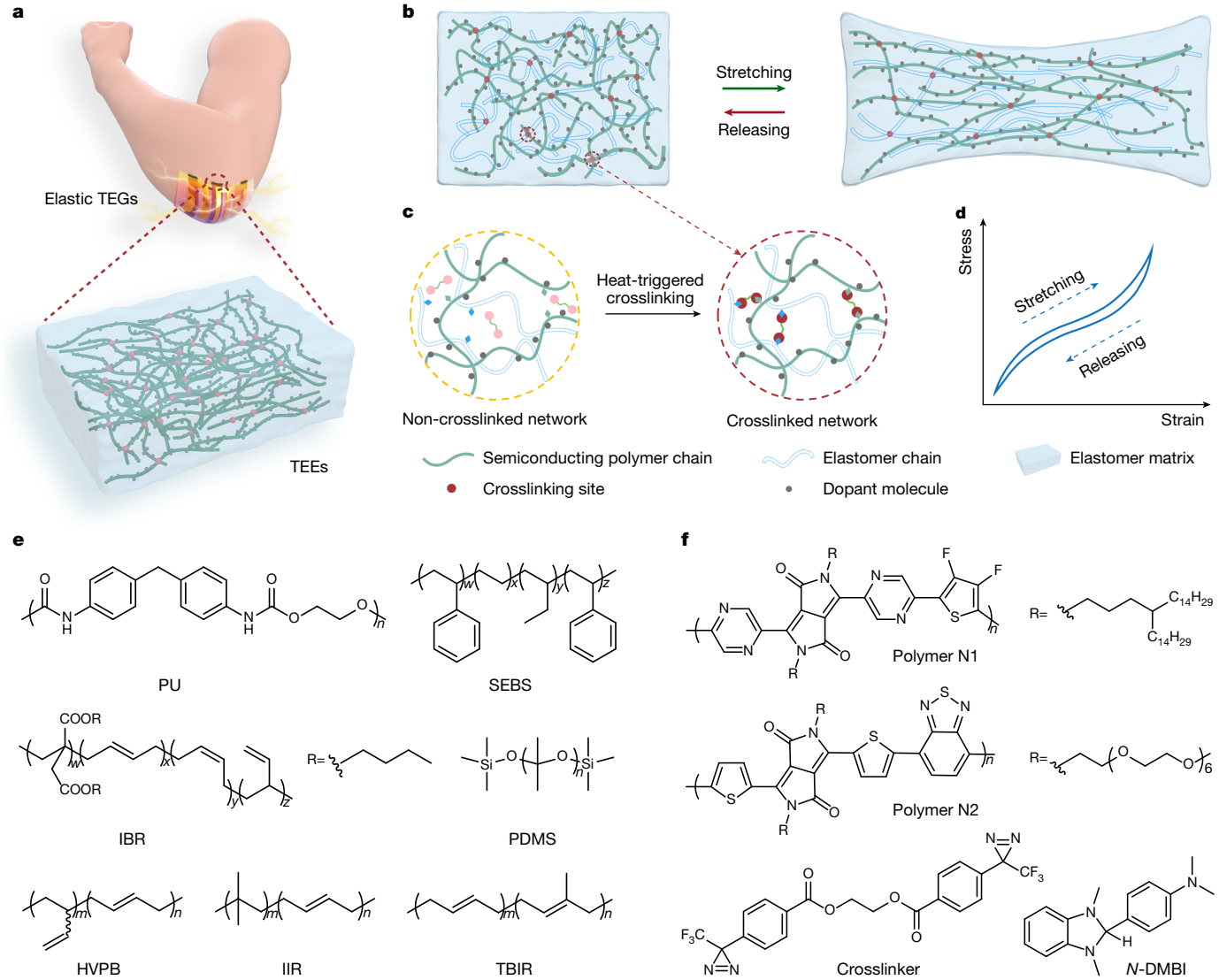

Fig. 1 | Schematic of our design strategy for TEEs. a, Schematic of an elastic TEG made by TEEs attached conformably to a bent human elbow. The diagram at the bottom shows the 3D architecture of TEEs, which are composed of self-assembled conjugated polymer nanofibres, an elastomer matrix, dopants and interchain crosslinking. **b**,**c**, Schematic of the size change of a TEE during the stretching–releasing process (**b**) and the thermally activatable crosslinking mechanism (**c**), in which the aliphatic C–H bonds on the conjugated polymer side chains and the elastomer might be involved. **d**, Typical stress–strain curve of our free-standing TEEs. A good elastomer requires high recovery and low energy loss during the stretching–releasing cycle. **e**, Chemical structures of the seven elastomers. **f**, Chemical structures of conjugated polymers N1 and N2, *bis*-diazirine crosslinker and n-dopant, *N*-DMBI.

extraordinary rubber-like recovery and high *ZT* values, reaching 0.49 at 300 K, coupled with unique strain-insensitive thermoelectric performance. Unlike conventional inorganic stretchable TEGs, which rely on complicated architectures and soft interconnects and have low fill factors due to rigid pillars[25,26], our TEE-based generators could enable superior epidermal conformability while maintaining high fill factors with reduced thermal resistance and heat loss.

Realization of uniform bulk nanophase separation

Integrating conjugated polymers with insulating elastomers constitutes a highly effective strategy for imparting stretchability to polymer semiconductors and is widely used in the fabrication of intrinsically stretchable organic field-effect transistors (OFETs)[20,27]. Unlike stretchable OFETs, which conduct charges solely at the interface and rely on substrate elasticity for shape recovery, elastic organic thermoelectrics require uniform bulk charge transport and necessitate the materials to be free-standing and intrinsically elastic. To address the outlined requirements and overcome the challenges posed by n-doping, we propose the following strategy for fabricating n-type TEEs (Fig. 1a–d): (1) using the Hansen solubility parameter (HSP) to predict the miscibility between conjugated polymers and insulating elastomers, thereby realizing a uniform bulk nanoscale phase separation; (2) using a thermally activable crosslinker to reinforce the polymer network and enhance the mechanical resilience of the composite; and (3) selecting thermally activable dopants that predominantly diffuse into the conjugated polymer-rich phase for targeted doping.

Seven insulating elastomers were purchased or synthesized for this study (Fig. 1e). Two n-type thermoelectric polymers, P(PzDPP-2FT) with hydrophobic alkyl side chains (denoted as N1) (ref. 24) and P(TDPP-BT-LEG) with hydrophilic ethylene glycol side chains (denoted as N2), were selected to demonstrate the above strategy (Fig. 1f, Supplementary Figs. 1–3, Supplementary Table 1 and Supplementary Note I for details). HSP provides a powerful predictive tool for polymer-solvent solubility and material miscibility[28]. We calculated the HSP values for

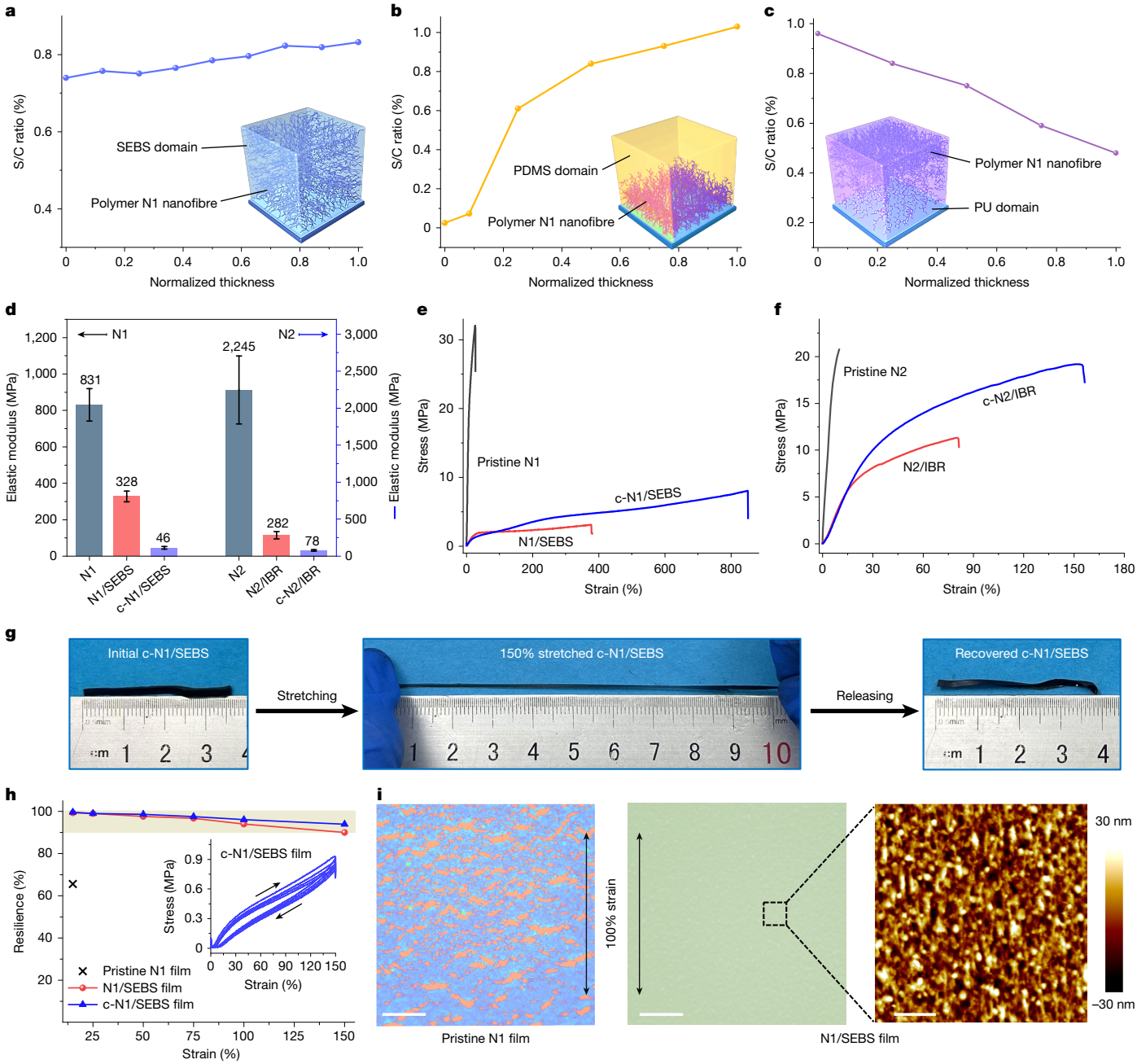

Fig. 2 | Characterization of the morphology and mechanical properties of the thermoelectric polymer/elastomer composites. a–**c**, Ratio changes between S(2*p*) and C(1*s*) peak (S/C ratio) obtained from the XPS profile element analysis of N1/SEBS (**a**), N1/PDMS (**b**) and N1/PU films (**c**) with a weight ratio of 7:3. Insets, the corresponding 3D illustrations of the vertical phase separation. **d**, Elastic moduli of N1, N2, N1/SEBS, N2/IBR, c-N1/SEBS and c-N2/IBR. Error bars represent the standard deviation of five measurements. **e**,**f**, Stress–strain curves of N1, N1/SEBS and c-N1/SEBS (**e**) and N2, N2/IBR and c-N2/IBR (**f**). **g**, Photos of the c-N1/SEBS under stretching and releasing. **h**, Elastic recovery rate of N1, N1/SEBS and c-N1/SEBS. Inset, the stretching–releasing cycles of c-N1/SEBS film. The elastic recovery rate (R) is defined as $R = \varepsilon_{recovered}/\varepsilon_{total} \times 100\%$, where ε_{total} is the maximum tensile strain applied and $\varepsilon_{recovered}$ is the strain recovered after unloading. **i**, Optical microscope images of pristine N1 (left), N1/SEBS (middle) and AFM height image of N1/ SEBS films (right) under 100% strain. Scale bars, 20 µm (left and middle); 2 µm (right).

the conjugated polymers and elastomers (Extended Data Fig. 1 and Supplementary Table 2). Polystyrene-*block*-poly(ethylene-*ran*-butylene)-*block*-polystyrene (SEBS) and itaconate-butadiene rubber (IBR) exhibited the smallest solubility distance (R_a) values when paired with polymers N1 and N2, respectively, indicating superior miscibility between the materials.

To validate the HSP predictions, we performed X-ray photoelectron spectroscopy (XPS) depth profile[27] and time-of-flight secondary ion mass spectrometry (ToF-SIMS) to characterize vertical phase separation (Fig. 2a–c and Extended Data Fig. 2). The N1/SEBS composite showed uniform bulk distribution of N1 nanofibres. By contrast, blending N1 with poly(dimethylsiloxane) (PDMS) and polyurethane (PU), both having large R_a values, resulted in vertical phase separation, which is strongly correlated with the surface energies of these materials. The polymers exhibit the following surface energy order: PU > trans-1,4-poly(butadiene-co-isoprene) rubber (TBIR) > polymer N1 ≈ SEBS > high vinyl polybutadiene rubber (HVPB) > butyl rubber (IIR) > PDMS (Supplementary Fig. 4). Blending with PDMS, having the lowest surface energy relative to N1, resulted in preferential N1 accumulation at the lower surface, whereas blending with PU, with the highest surface energy,

caused progressive N1 depletion from the top to the bottom surface. Morphological analysis of the top and bottom surfaces of the composites further confirmed this vertical phase separation (Supplementary Figs. 5 and 6). Similar phase separation behaviour was seen in N2 composites. Blending with IBR enabled the formation of a uniformly dispersed N2 nanofibre network. The uniform bulk nanophase separation in both N1/SEBS and N2/IBR composites can boost mechanical toughness and strain recovery[29].

Thermally activable crosslinking to improve elasticity

Interchain sliding always occurs during the deformation of conjugated polymers. We predicted that the crosslinking of conjugated polymers with elastomer matrices could enhance the elasticity of composites. We designed a *bis*-diazirine crosslinker that decomposed thermally or photolytically into carbenes (Fig. 1f and Supplementary Fig. 7). These reactive species chemically crosslinked aliphatic sidechains of conjugated polymers with elastomers by selective reaction with C(sp^3)–H bonds[30]. After forming uniform bulk nanophase separation, the composite exhibited a marked reduction in elastic modulus and substantial enhancement in tensile strain (Fig. 2d–f and Supplementary Fig. 8). Subsequent crosslinking with *bis*-diazirine further decreased elastic modulus while amplifying tensile strain.

The pristine N1 sustained a tensile strain of only <25%. The formation of uniform bulk nanophase separation increased the tensile strain of the composites to 375%. Further crosslinking with 5 wt% crosslinker (denoted as c-N1/SEBS) yielded unprecedented strain exceeding 850% (Supplementary Video 1). This extreme strain tolerance provides design redundancy for wearable applications and ensures consistent functionality under diverse deformations. According to the American Society of Testing Materials (ASTM) D1566, an elastomer or rubber is required to retract within 1 min to less than 1.5 times its initial length after being stretched to 100% strain and maintained for 1 min. c-N1/SEBS was tested following this protocol and recovered to less than 1.1 times its initial length (Fig. 2g and Supplementary Video 2), demonstrating its mechanical property comparable to or superior to traditional rubbers. Similarly, the crosslinked N2/IBR composite (denoted as c-N2/IBR) exhibited a tensile strain of up to 150%, nearly 20 times higher than the pristine N2. The mechanical properties of the N2 composites were inferior to those of the N1 composites, mainly because of the inherently higher crystallinity of N2.

Moreover, crosslinked N1 and N2 composites showed significantly reduced hysteresis and energy loss (Supplementary Figs. 9–11 and Supplementary Tables 3 and 4). The c-N1/SEBS exhibited outstanding elastic resilience of >90% with <25% energy loss even under 150% strain (Fig. 2h, Extended Data Fig. 3 and Supplementary Video 3). To our knowledge, this is the first free-standing polymer semiconductors that can sustain >90% elastic recovery rate beyond 100% strain. Similarly, the c-N2/IBR also showed substantially improved elastic resilience and reduced energy loss. We attribute these enhancements to crosslinking-induced restriction of interchain polymer slippage.

We also explored the microstructural and molecular-level changes of the composites under strains[31] (Fig. 2i and Supplementary Figs. 12–15). Unlike the pristine N1 and N2 films with numerous micro-sized cracks under strains, the N1/SEBS and N2/IBR composite films displayed no discernible cracks even at the nanoscale level while exhibiting a pronounced polymer chain alignment along the stretching direction. Therefore, the pristine film withstands tensile stress by crack propagation, whereas the composite film mitigates fracture damage through strain-induced polymer chain rearrangement. Absorption spectra and grazing incidence wide-angle X-ray scattering (GIWAXS) showed that the π–π stacking distance of conjugated polymers diminished after incorporating the elastomers (Supplementary Figs. 16–18 and Supplementary Table 5). Complementary molecular dynamics simulations indicated that the reduced π–π stacking distance could enhance the polymer backbone planarity and reinforce interchain coupling (Supplementary Fig. 19). These findings indicate that the considerable mechanical enhancements stem from the optimized polymer arrangement and increased interchain interaction, which, we shall prove later, can also enhance charge transport.

Targeted n-doping and thermoelectric performance

We screened several n-dopants and found that the thermally activatable n-dopants (such as TAM[32] and *N*-DMBI[33]) could effectively dope pristine N1 after thermal activation at 120 °C (Fig. 1f and Supplementary Figs. 20–22). However, upon incorporating SEBS, the TAM-doped N1/SEBS composite displayed a notably decreased electrical conductivity (σ) from over 20 S cm^{-1} to 0.38 S cm^{-1}, whereas the *N*-DMBI-doped N1/SEBS achieved a higher σ (65.9 S cm^{-1}) than doped N1 alone (43.9 S cm^{-1}) (Fig. 3a). To investigate the differential doping behaviours of *N*-DMBI and TAM, we performed molecular dynamics simulations in N1/SEBS system. Compared with TAM, *N*-DMBI exhibited a closer association with the N1 polymer backbone, indicating stronger molecular interactions with N1 (Fig. 3b and Supplementary Figs. 23 and 24). Atomic force microscopy coupled with infrared spectroscopy (AFM-IR) analysis further showed the preferential aggregation of *N*-DMBI on conjugated polymer nanofibres rather than elastomer regions (Fig. 3c and Supplementary Figs. 25 and 26). Dynamic light scattering measurement showed that adding *N*-DMBI into the conjugated polymer solution reduced the size of polymer aggregates, also corroborating the strong conjugated polymer–*N*-DMBI interactions (Supplementary Fig. 27). Thus, we conclude that stronger interactions between the conjugated polymer backbone and *N*-DMBI promote targeted diffusion into the conjugated polymer-rich phase, enhancing doping efficiency while preserving nanophase separation. With increasing *N*-DMBI doping concentration, the polaron absorption peak in the composite intensified (Supplementary Fig. 28), indicating effective n-doping even at elevated dopant levels.

To evaluate thermoelectric performance, a bottom-contact device configuration was used because of its ease of integration and better performance relative to top-contact device (Supplementary Fig. 29). After doping with *N*-DMBI, the composites demonstrated significantly enhanced σ and PF values compared with their pristine polymers (Supplementary Figs. 30–33 and Supplementary Table 6). The doped N1/SEBS composite (denoted as TEE-1) exhibited a higher PF of 87.5 μW m^{-1} K^{-2} than pristine N1 (56.9 μW m^{-1} K^{-2}). Owing to the inherently high Seebeck coefficient (S) of N2, the doped N2/IBR composite (denoted as TEE-2) achieved a higher PF of 514 μW m^{-1} K^{-2}, representing a milestone among reported n-type thermoelectric polymers (Fig. 3d). Except for targeted enhanced doping levels, we observed that although incorporating insulating elastomers diluted the active component, the formation of uniform polymer nanofibre networks and decreased π–π stacking distance collectively increased charge carrier mobility (Supplementary Figs. 34–37 and Supplementary Tables 7–9).

We further explored the effects of incorporating elastomers on the thermal conductivity (κ) of the composites. The total κ was calculated as the sum of electronic thermal conductivity (κ_e) and phonon thermal conductivity (κ_{ph}), expressed as $\kappa = \kappa_e + \kappa_{ph}$ (refs. 34,35) (Supplementary Fig. 38 and Supplementary Note II for details). The calculated κ values were within a reasonable range among the reported organic thermoelectric materials (Fig. 3e, Supplementary Fig. 39 and Supplementary Table 10). Notably, TEE-1 exhibited an approximately 17% reduction in κ relative to doped N1, whereas TEE-2 showed about 50% reduction in κ compared with doped N2. Scanning thermal microscopy results showed significantly higher 3ω (third-harmonic frequency) voltages in the TEE films than in the pristine polymer films, indicating lower thermal conductivity in the composites[36] (Fig. 3f). We attribute this substantial thermal conductivity reduction to two primary factors:

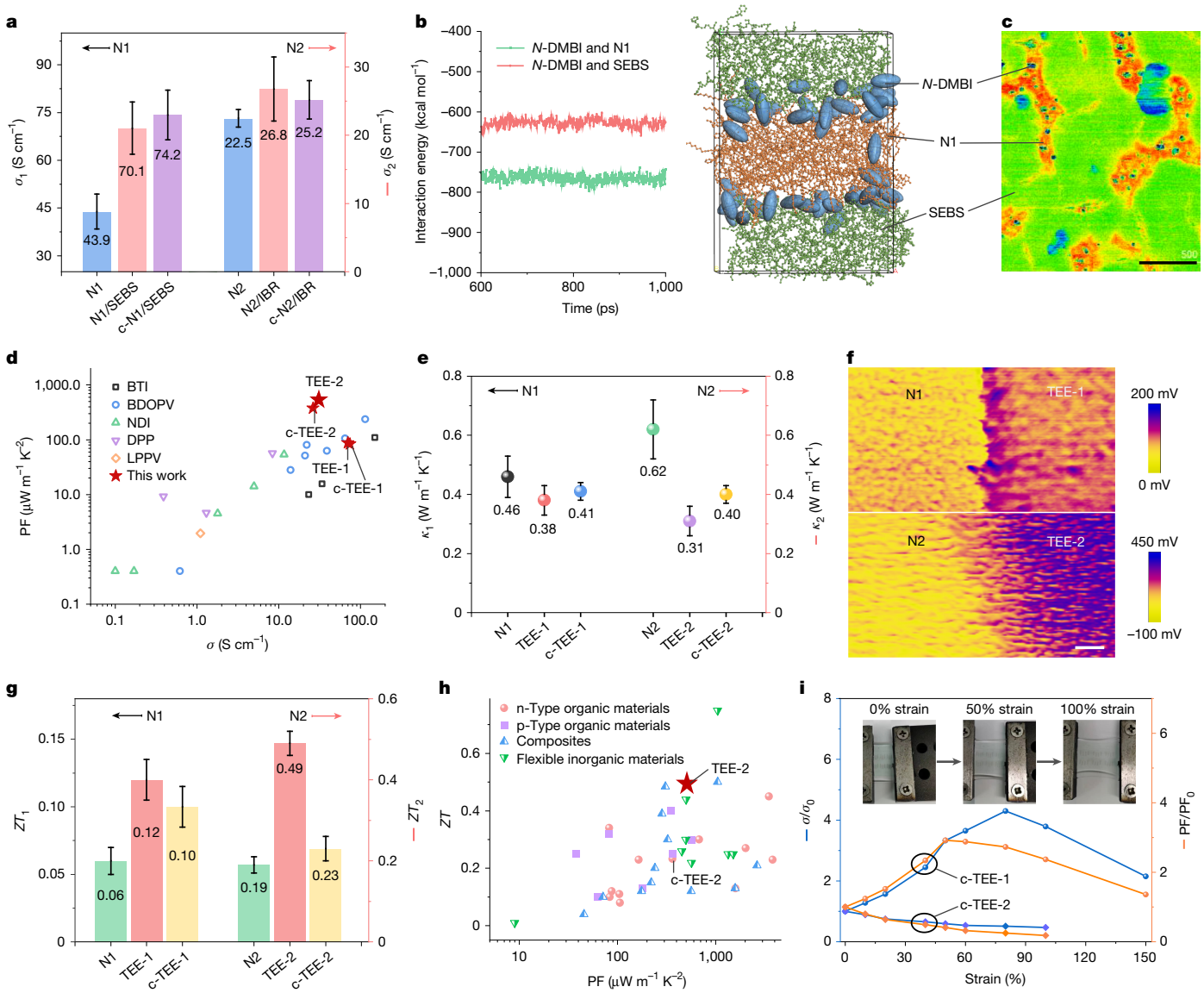

Fig. 3 | Dopant selection and thermoelectric property characterization. **a**, Electrical conductivity of *N*-DMBI-doped N1, N1/SEBS and c-N1/SEBS, and N2, N2/IBR and c-N2/IBR. Error bars represent the standard deviation of five measurements. **b**, Non-bonding energy of *N*-DMBI/N1 and *N*-DMBI/SEBS (left), and equilibrium configurations of the N1/SEBS/*N*-DMBI blend system (right) calculated by molecular dynamics simulations. **c**, AFM-IR image of the N1/SEBS composite doped with 90 mol% *N*-DMBI. **d**, Comparison of the PFs with electrical conductivities for our TEE and c-TEE and previously reported n-type organic thermoelectric polymers. **e**, Thermal conductivity of the doped N1, TEE-1 and c-TEE-1, and doped N2, TEE-2 and c-TEE-2. Error bars represent the standard deviation of three measurements. **f**, Comparison of the nanoresolved 3ω scanning thermal microscopy thermal maps of N1 and TEE-1 with N2 and TEE-2. **g**, *ZT* values of the doped N1, TEE-1 and c-TEE-1, and doped N2, TEE-2 and c-TEE-2. Error bars represent the standard deviation of three measurements. **h**, Comparison of the *ZT* and PF values for state-of-the-art flexible inorganic and organic thermoelectric materials. The detailed data are summarized in Supplementary Table 11. **i**, Electrical conductivity change (σ/σ_0) and PF change (PF/PF$_0$) of the c-TEE films under different strains parallel to the charge transport direction. Inset, photos of the custom-made stretching station during measurement. Scale bars, 500 nm (**c**); 2 μm (**f**).

(1) the incorporation of elastomers with intrinsically low κ values and (2) enhanced interfacial scattering of propagans resulting from uniform polymer nanofibres and nanophase separation[36,37] (Supplementary Note III).

The synergistic effects of increased charge transport and decreased thermal conductivity yielded *ZT* values of the composites exceeding twice those of the pristine polymers (Fig. 3g). TEE-2 achieved a peak *ZT* value of 0.49 at 300 K, which is among the highest reported for organic thermoelectric materials[15,38] and comparable to state-of-the-art ductile inorganic counterparts[3] (Fig. 3h, Supplementary Fig. 40 and Supplementary Table 11). Although chemical crosslinking may disrupt charge transport pathways and diminish phonon scattering efficiency, the doped crosslinked composites maintained outstanding thermoelectric performance. For instance, c-TEE-2 demonstrated a high PF value of 363 μW m^{-1} K^{-2} and a *ZT* value of 0.23 at 300 K. Furthermore, c-TEEs exhibited strain-independent electrical properties comparable or superior to the best-reported stretchable polymer conductors[20,39–43] (Supplementary Figs. 41 and 42 and Supplementary Table 12). On stretching, TEE-1 and c-TEE-1 maintained largely increased σ even at 150% strain, whereas the σ of N1 decreased sharply, by more than 25 times under 100% strain (Supplementary Fig. 43). Despite strain-dependent reduction in the *S* of TEE-1 and c-TEE-1 (Supplementary Fig. 44), their PF remained elevated under strains because of the dominant contribution of the enhanced σ (Fig. 3i). Likewise, c-TEE-2 exhibited substantially improved strain-insensitive σ and PF compared with pristine N2 (Supplementary Fig. 45).

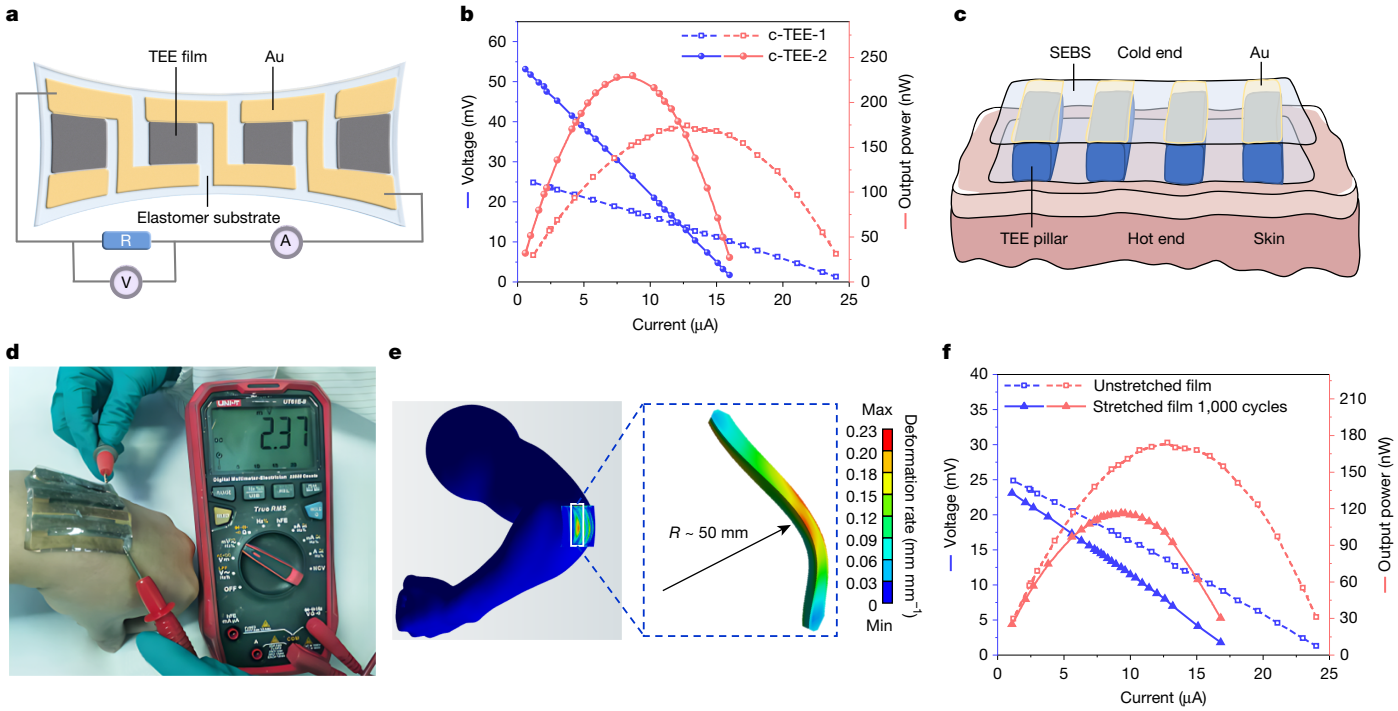

Fig. 4 | Fabrication and measurement of the intrinsically elastic TEGs. **a**, Schematic of the measurement setup of the in-plane elastic TEGs. **b**, Output voltage and power of the in-plane elastic TEGs. The given temperature gradient between the hot and cold sides is 48 K. **c**, Device structure of the out-of-plane elastic TEGs—conformally adhering to human skin. **d**, Photograph showing the open-circuit voltage of the out-of-plane elastic TEG made by c-TEE-2 when attached to a bending wrist. **e**, Finite-element analysis to evaluate the strain changes of the c-TEE pillars on a bending elbow. **f**, Output voltage and power of the in-plane elastic TEGs without stretching and after 1,000 stretching–releasing cycles at 25% strain. The given temperature gradient between the hot and cold sides is 48 K.

Fabrication of elastic TEGs

Using the c-TEEs, we fabricated in-plane elastic TEGs (Fig. 4a and Supplementary Fig. 46). Under a temperature gradient of 48 K, these TEGs achieved maximum power outputs of 174 nW and 229 nW using c-TEE-1 and c-TEE-2 as the thermoelectric legs, respectively (Fig. 4b and Supplementary Tables 13 and 14). When configured with skin and atmosphere as the hot and cold side (ΔT = 4 K), the TEG generated an output voltage of 1.30 mV, promising to power low-power-consumption biosensors[44] (Supplementary Fig. 47 and Supplementary Note IV). To sufficiently substantiate the mechanical merits of c-TEEs, we developed out-of-plane elastic TEGs, featuring both vertical heat and current flow (Fig. 4c and Supplementary Figs. 48 and 49). These devices necessitate the TEE pillars free-standing and vertically aligned, interconnected by patterned microcracked gold electrodes on a thin SEBS film (<100 μm). The TEGs conform seamlessly to the human wrist, delivering a high output voltage of 2.37 mV (Fig. 4d), comparable to state-of-the-art ductile inorganic TEGs[3]. They also maintain stable voltage output during dynamic wrist and elbow bending (Supplementary Fig. 50). We conducted a finite-element simulation to assess the deformation of thermoelectric pillars attached to a human elbow with a 50-mm bending radius, showing a maximum tensile strain of 23% (Fig. 4e). This tensile deformation is unachievable with traditional organic and inorganic thermoelectric materials. Moreover, both in-plane and out-of-plane elastic TEGs maintained high output voltages under diverse deformations or cyclic stretching (Fig. 4f and Supplementary Videos 4 and 5).

Unlike rigid inorganic architectures requiring sophisticated stretchable interconnects for strain accommodation[25,26], the inherent stretchability and elasticity of c-TEE pillars allow for a denser arrangement of active thermoelectric material. This configuration could achieve higher fill factors, reduce parasitic heat losses and ultimately enhance energy conversion efficiency. Furthermore, the low Young's modulus (<100 MPa) of c-TEEs combined with the thin SEBS supporting layer can minimize the air gap and device–skin thermal resistance[45] (for more detailed analysis, see Supplementary Note V). Although out-of-plane configurations exhibit lower thermoelectric performance than their in-plane counterparts now, primarily attributed to suboptimal polymer alignment (Supplementary Fig. 51), they offer superior practical advantages for skin-integrated energy harvesting in real-world wearable scenarios[46]. Their performance can be further enhanced through innovative fabrication approaches such as 3D printing (Supplementary Fig. 52).

In summary, we present a general approach for developing TEEs through three synergistic design principles: (1) uniform bulk nanophase separation; (2) thermally activated crosslinking; and (3) strategic dopant selection. This approach achieves simultaneous optimization of mechanical properties and thermoelectric performance. The resulting TEEs establish a material platform for elastic TEGs that combine epidermal compliance and potentially higher heat harvesting efficiency, bridging the gap between human-compatible mechanics and efficient energy harvesting in next-generation self-powered wearable electronics.

Online content

Any methods, additional references, Nature Portfolio reporting summaries, source data, extended data, supplementary information, acknowledgements, peer review information; details of author contributions and competing interests; and statements of data and code availability are available at https://doi.org/10.1038/s41586-025-09387-z.

1. Hou, C. & Zhu, M. Semiconductors flex thermoelectric power. *Science* **377**, 815–816 (2022).
2. Hong, S. et al. Wearable thermoelectrics for personalized thermoregulation. *Sci. Adv.* **5**, eaaw0536 (2019).

3. Yang, Q. et al. Flexible thermoelectrics based on ductile semiconductors. *Science* **377**, 854–858 (2022).
4. Wei, T.-R. et al. Exceptional plasticity in the bulk single-crystalline van der Waals semiconductor InSe. *Science* **369**, 542–545 (2020).
5. Bell, L. E. Cooling, heating, generating power, and recovering waste heat with thermoelectric systems. *Science* **321**, 1457–1461 (2008).
6. Shi, X.-L., Zou, J. & Chen, Z. G. Advanced thermoelectric design: from materials and structures to devices. *Chem. Rev.* **120**, 7399 (2020).
7. Shi, X. & He, J. Thermopower and harvesting heat. *Science* **371**, 343–344 (2021).
8. Jia, Y. et al. Wearable thermoelectric materials and devices for self-powered electronic systems. *Adv. Mater.* **33**, 2102990 (2021).
9. Bahk, J.-H., Fang, H., Yazawa, K. & Shakouri, A. Flexible thermoelectric materials and device optimization for wearable energy harvesting. *J. Mater. Chem. C* **3**, 10362–10374 (2015).
10. Peng, J. et al. 3D extruded composite thermoelectric threads for flexible energy harvesting. *Nat. Commun.* **10**, 5590 (2019).
11. Han, S. et al. Multiscale nanowire-microfluidic hybrid strain sensors with high sensitivity and stretchability. *npj Flex. Electron.* **2**, 16 (2018).
12. Qin, B. et al. Moving fast makes for better cooling: optimizing carrier mobility with composition and processing is key for thermoelectric coolers. *Science* **378**, 832–833 (2022).
13. Mallick, M. M. et al. High figure-of-merit telluride-based flexible thermoelectric films through interfacial modification via millisecond photonic-curing for fully printed thermoelectric generators. *Adv. Sci.* **9**, 2202411 (2022).
14. Tian, Y. et al. Facile fabrication of flexible and high-performing thermoelectrics by direct laser printing on plastic foil. *Adv. Mater.* **36**, 2307945 (2024).
15. Gao, H. et al. Transition metal-catalysed molecular n-doping of organic semiconductors. *Nature* **599**, 67–73 (2021).
16. Feng, K., Guo, H., Sun, H. & Guo, X. N-type organic and polymeric semiconductors based on bithiophene imide derivatives. *Acc. Chem. Res.* **54**, 3804–3817 (2021).
17. Zheng, Y.-Q. et al. Monolithic optical microlithography of high-density elastic circuits. *Science* **373**, 88–94 (2021).
18. Jiang, Y. et al. A universal interface for plug-and-play assembly of stretchable devices. *Nature* **614**, 456–462 (2023).
19. Zhang, Z. et al. High-brightness all-polymer stretchable LED with charge-trapping dilution. *Nature* **603**, 624–630 (2022).
20. Zhong, D. et al. High-speed and large-scale intrinsically stretchable integrated circuits. *Nature* **627**, 313–320 (2024).
21. Kim, N. et al. Elastic conducting polymer composites in thermoelectric modules. *Nat. Commun.* **11**, 1424 (2020).
22. Tseng, C.-C. et al. Intrinsically stretchable organic thermoelectric polymers enabled by incorporating fused-ring conjugated breakers. *Small* **20**, 2401966 (2024).
23. Wang, S., Zuo, G., Kim, J. & Sirringhaus, H. Progress of conjugated polymers as emerging thermoelectric materials. *Prog. Polym. Sci.* **129**, 101548 (2022).
24. Yan, X. et al. Approaching disorder-tolerant semiconducting polymers. *Nat. Commun.* **12**, 5723 (2021).
25. Han, Y., Tetik, H. & Malakooti, M. H. 3D soft architectures for stretchable thermoelectric wearables with electrical self-healing and damage tolerance. *Adv. Mater.* **36**, 2407073 (2024).
26. Han, Y., Simonsen, L.-E. & Malakooti, M. H. Printing liquid metal elastomer composites for high-performance stretchable thermoelectric generators. *Adv. Energy Mater.* **12**, 2201413 (2022).
27. Xu, J. et al. Highly stretchable polymer semiconductor films through the nanoconfinement effect. *Science* **355**, 59–64 (2017).
28. Anwar, O. et al. Hansen parameter evaluation for the characterization of titania photocatalysts using particle size distributions and combinatorics. *Nanoscale* **14**, 13593–13607 (2022).
29. Fernández-Rico, C. et al. Elastic microphase separation produces robust bicontinuous materials. *Nat. Mater.* **23**, 124–130 (2023).
30. Lepage, M. L. et al. A broadly applicable cross-linker for aliphatic polymers containing C-H bonds. *Science* **366**, 875–878 (2019).
31. Wu, H.-C. et al. A rapid and facile soft contact lamination method: Evaluation of polymer semiconductors for stretchable transistors. *Chem. Mater.* **26**, 4544–4551 (2014).
32. Yang, C.-Y. et al. A thermally activated and highly miscible dopant for n-type organic thermoelectrics. *Nat. Commun.* **11**, 3292 (2020).
33. Wei, P., Oh, J. H., Dong, G. & Bao, Z. Use of a 1*H*-benzoimidazole derivative as an *n*-type dopant and to enable air-stable solution-processed *n*-channel organic thin-film transistors. *J. Am. Chem. Soc.* **132**, 8852–8853 (2010).
34. Liu, J. et al. Thermal conductivity and elastic constants of PEDOT:PSS with high electrical conductivity. *Macromolecules* **48**, 585–591 (2015).
35. Brunetti, I., Dash, A., Scheunemann, D. & Kemerink, M. Is the field of organic thermoelectrics stuck? *J. Mater. Res.* **39**, 1197–1206 (2024).
36. Wang, D. et al. Multi-heterojunctioned plastics with high thermoelectric figure of merit. *Nature* **632**, 528–535 (2024).
37. Qian, X., Zhou, J. & Chen, G. Phonon-engineered extreme thermal conductivity materials. *Nat. Mater.* **20**, 1188–1202 (2021).
38. Fan, Z., Du, D., Guan, X. & Ouyang, J. Polymer films with ultrahigh thermoelectric properties arising from significant Seebeck coefficient enhancement by ion accumulation on surface. *Nano Energy* **51**, 481–488 (2018).
39. Jiang, Y. et al. Topological supramolecular network enabled high-conductivity, stretchable organic bioelectronics. *Science* **375**, 1411–1417 (2022).
40. Zhou, T. et al. 3D printable high-performance conducting polymer hydrogel for all-hydrogel bioelectronic interfaces. *Nat. Mater.* **22**, 895–902 (2023).
41. He, H. et al. Salt-induced ductilization and strain-insensitive resistance of an intrinsically conducting polymer. *Sci. Adv.* **8**, eabq8160 (2022).
42. Wei, H. et al. Orthogonal photochemistry-assisted printing of 3D tough and stretchable conductive hydrogels. *Nat. Commun.* **12**, 2082 (2021).
43. Chen, X.-X. et al. High-mobility semiconducting polymers with different spin ground states. *Nat. Commun.* **13**, 2258 (2022).
44. Nan, K. et al. Compliant and stretchable thermoelectric coils for energy harvesting in miniature flexible devices. *Sci. Adv.* **4**, eaau5849 (2018).
45. Lv, H. et al. A flexible spring-shaped architecture with optimized thermal design for wearable thermoelectric energy harvesting. *Nano Energy* **88**, 106260 (2021).
46. Tian, Y. & Molina-Lopez, F. Boosting the performance of printed thermoelectric materials by inducing morphological anisotropy. *Nanoscale* **13**, 5202–5215 (2021).

Publisher's note Springer Nature remains neutral with regard to jurisdictional claims in published maps and institutional affiliations.

Springer Nature or its licensor (e.g. a society or other partner) holds exclusive rights to this article under a publishing agreement with the author(s) or other rightsholder(s); author self-archiving of the accepted manuscript version of this article is solely governed by the terms of such publishing agreement and applicable law.

© The Author(s), under exclusive licence to Springer Nature Limited 2025

Methods

All details of materials synthesis, device preparation and performance characterizations are provided in the Supplementary Information.

Materials

Poly(pyrazine-diketopyrrolopyrrole-3,4-difluorothiophene) (PzDPP-2FT, denoted as N1) was synthesized following our previously reported method[24]. Poly(thiophene-diketopyrrolopyrrole-benzothiadiazole) (P(TDPP-BT-LEG), denoted as N2) was synthesized using the procedure described in the Supplementary Information. 4-(1,3-Dimethyl-2,3-dihydro-1H-benzoimidazol-2-yl)phenyl)dimethylamine (*N*-DMBI), cobaltocene (Cp_2Co) and tetrakis-(dimethylamino)ethylene (TDAE) were purchased from Sigma-Aldrich. Trisaminomethane derivative (TAM) was synthesized according to the method reported in ref. 32. SEBS (H1221, with a poly(ethylene-co-butylene) volume fraction of 88%) was purchased from Asahi Kasei. Poly(dimethylsiloxane) (PDMS, Sylgard 184) was purchased from Dow Corning. Polyurethane (PU) was provided by Youzhan New Material. High vinyl polybutadiene rubber (HVPB), butyl rubber (IIR), trans-1,4-poly(butadiene-co-isoprene) rubber (TBIR) and itaconate-butadiene rubber (IBR) were synthesized following the methods described in the Supplementary Information. All the elastomers were purified by precipitation and filtration in ethanol three times before use. Carbon nanotubes (P3-SWNTs) used for the preparation of stretchable electrodes were purchased from Carbon Solutions. All the processing solvents, such as octadecyl trichlorosilane, chlorobenzene, cyclohexane, 1-propanol, acetone and toluene, were purchased from Sigma-Aldrich and used as received.

Preparation of N1/elastomer composite films

Polymer N1 solution (8 mg ml^{-1}) was obtained by dissolving N1 in chlorobenzene at 80 °C. The elastomer solution (30 mg ml^{-1} in chlorobenzene) was obtained by dissolving PDMS (base/crosslinker = 10:1 wt/wt) at room temperature or dissolving other elastomers (including SEBS, PU, HVPB, IIR and TBIR) at 80 °C. All the solutions were stirred for 1 h. After that, the N1/elastomer blended solutions with a weight ratio of 7:3 were prepared at room temperature (for PDMS only) or at 80 °C for 30 min. Subsequently, the polymer/elastomer solutions were subjected to spin-coating on glass substrates at 2,000 rpm for 60 s, and then annealed at 120 °C for 30 min in a nitrogen-filled glovebox. The prepared N1/elastomer composite films were used for morphology analysis and conductivity measurements.

Preparation of N2/elastomer composite films

The N2/elastomer blended solutions were obtained by mixing polymer N2 solution (8 mg ml^{-1} in chloroform) with elastomers (including IBR, PDMS and PU) solution (30 mg ml^{-1} in chloroform). The mixture was stirred at 50 °C for 30 min. The composite films were then prepared using the same procedures as the N1/elastomer composite films.

Fabrication of in-plane elastic TEG

The fabrication procedure of the intrinsically elastic TEG based on the in-plane structure is shown in Supplementary Fig. 46. TPU solution (10 ml; 150 mg ml^{-1} in tetrahydrofuran) was poured onto a square glass sheet with a side length of 5 cm, followed by slow evaporating in a fume hood at room temperature for 3 h. The as-prepared TPU film, with an approximate thickness of 500 μm, was gently peeled off the glass sheet for the thermal evaporation of Au electrodes. A 50-nm layer of interpenetrating gold electrodes was deposited on the TPU film at a rate of 0.3 Å s^{-1} using a shadow mask. Then, the substrate was cleaned by plasma treatment for 1 min. Finally, the thermoelectric polymer composite was deposited by drop-casting and annealed at 120 °C for 2 h under a nitrogen atmosphere. Each thermoelectric module has a length (l) of 8 mm and a width (w) of 5 mm. The output power of the elastic TEG was measured in a nitrogen-filled glovebox according to the method reported in ref. 47. We recorded the circuit current and voltage using a multimeter (UT890D).

Fabrication of out-of-plane elastic TEG

The intrinsically elastic TEG based on the out-of-plane structure was fabricated using a transfer-layer lamination process, with serially connected n-type thermoelectric pillars (Supplementary Fig. 48). The stretchable SEBS films, with an approximate thickness of 0.1 mm, were prepared by drop-coating a SEBS-H1221 solution (100 mg ml^{-1} in toluene) onto an octadecyltrichlorosilane (OTS)-treated glass substrate and then cured at 70 °C for 1 h. The patterned microcracked Au electrodes were prepared through the thermal deposition of Au onto the SEBS film at an evaporation rate of 0.3 Å s^{-1}, using a shadow mask. The thickness of the Au film is approximately 50 nm. The TEE pillars were prepared by drop-coating a TEE solution into a polytetrafluoroethylene (PTFE) template and then thermally annealed at 120 °C for 1 h. The thickness of the TEE pillars is approximately 2 mm. The thermoelectric pillars were peeled off the PTFE template and transferred onto the bottom SEBS film with patterned gold electrodes. Microcracked gold electrodes were fabricated, and TEE pillars were connected in series using thin SEBS films as the supporting layer. After that, the top SEBS film, patterned with gold electrodes, was laminated onto the bottom SEBS film with TEE pillars. To improve the adhesion between the SEBS film and the TEE pillars, the device was subjected to thermal annealing for 30 min under a vacuum at 80 °C.

Film morphology characterization

Surface morphologies of polymer films were analysed using an Olympus BX53 cross-polarized optical microscope and a NanoMan VS AFM operating in the tapping mode. The polymer film thickness was determined by AFM or a step profiler (Dektak-XT, Bruker) with a stylus force of 0.1 mg and a scanning speed of 30 μm s^{-1}. The molecular orientation alignment under stretching was intuitively observed by AFM height and phase images. The in-depth element analysis of the microphase separation in semiconducting polymer nanofibres was performed using XPS on the ESCALAB 250Xi XPS microprobe equipped with an Ar 2000 gas cluster ion beam gun. The sulfur (S) elements merely exist in the conjugated polymers N1 and N2. Thus, the S(2*p*) peak relative to the C(1*s*) peak was used to quantitatively express the distribution of polymer nanofibres in the elastomer matrix.

Polymer aggregation and molecular packing analysis

Polymer aggregation and doping efficiency were analysed using ultraviolet–visible–NIR absorption spectroscopy (SHIMADZU 2600 spectrophotometer). To verify the molecular orientation alignment under tensile strain, the spectrophotometer equipped with a rotational polarizer was used to characterize the absorption intensity of polymer films along and perpendicular to the stretching direction. The molecular stacking of polymer composite films with various elastomer contents was investigated through GIWAXS performed on a Xenocs Xuess 2.0 beamline, with an incident X-ray angle of 0.2° and a wavelength of 1.54 Å. The scattering signals were recorded by a Pilatus 1M detector with a distance of about 131 mm from the samples. The diffraction peak areas were numerically integrated using the Nika software package for use with Wavemetrics Igor and WAXS tools.

Polymer-dopant and elastomer-dopant interaction analysis

The polymer-dopant and elastomer-dopant interactions were explored using dynamic light scattering, which was recorded from a nanoparticle size and potential analyser (Malvern Zetasizer Nano ZS90) at a wavelength of 633 nm. The solution concentration of the polymer composites was adjusted to 0.01 mg ml^{-1} in chlorobenzene. The measured particle diameter ranges from 0.1 nm to 10^4 nm. The polymer-dopant interaction was determined by comparing the position and intensity of particle diameter peaks of polymer solutions with or without *N*-DMBI.

The polymer-dopant and elastomer-dopant interactions were also analysed using molecular dynamics simulations (for details, see the Supplementary Information).

Thermoelectric performance measurement

The electrical conductivity (σ) and Seebeck coefficient (S) measurements were conducted according to the methods reported in the in-plane direction[48]. The PF was calculated using the equation PF = σS^2. The σ value was recorded from a Keithley 4200 SCS semiconductor analyser based on a co-linear four-point-probe bar geometry. The Seebeck coefficient S was calculated using the equation $S = \Delta V_{\mathrm{therm}}/\Delta T$, where $\Delta V_{\mathrm{therm}}$ represents the thermal voltage between the hot and cold ends at a temperature gradient ΔT. The thermal voltage $\Delta V_{\mathrm{therm}}$ was collected by a Keithley 4200 SCS.

The precise determination of thermal conductivity (κ) in n-type thermoelectric polymers poses a marked challenge, as these materials are prone to air-induced de-doping. This de-doping can result in an underestimation of the electronic thermal conductivity (κ_e). The accurate measurement of κ_e currently stands as a formidable task (Supplementary Note II). To more accurately determine the thermal conductivity (κ), we initially calculated the κ_e by leveraging the Wiedemann–Franz law using the following equation[35]:

$$\kappa_e = L\sigma T$$

where σ represents the electrical conductivity, T represents the thermodynamic temperature and L is the Lorentz constant, 2.45×10^{-8} W Ω K^{-2}. Then, we measured the phonon thermal conductivity (κ_{ph}) on a Linseis thin film analyser (Linseis TFA) using a 3ω method[36,49]. The κ value was determined by combining the κ_{ph} and κ_e according to the following formula:

$$\kappa = \kappa_{ph} + \kappa_e$$

Briefly, the polymer films were subjected to spin-coating onto a thermal conductivity measurement chip integrated with two suspended SiN_x membranes in a nitrogen-filled glovebox. The suspended membranes were transferred into the Linseis TFA, followed by vacuum pumping. Before the in-plane thermal conductivity measurement, the polymer films were thermally annealed at 120 °C for 30 min to activate the doping process. The film thickness was about 500 nm. The thermal conductivity was analysed by a built-in software from the Linseis TFA setup. Meanwhile, we have statistically analysed the electric conductivity and thermal conductivity data of organic thermoelectric materials in the literature, as shown in Supplementary Fig. 39 and Supplementary Table 10, further confirming that our thermal conductivity data are within a reasonable range.

The thermoelectric conversion efficiency is evaluated by the in-plane thermoelectric figure of merit (ZT):

$$ZT = \frac{S^2\sigma}{\kappa}T$$

where T represents the absolute temperature.

Data availability

All data supporting the findings of this study are available in the paper and its Supplementary Information. Other related raw data are fully and freely available from the corresponding author at the point of publication. Source data are provided with this paper.

47. Yu, Z.-D. et al. High n-type and p-type conductivities and power factors achieved in a single conjugated polymer. *Sci. Adv.* **9**, eadf3495 (2023).
48. Lu, Y. et al. Rigid coplanar polymers for stable n-type polymer thermoelectrics. *Angew. Chem. Int. Ed.* **58**, 11390–11394 (2019).
49. Liu, J. et al. N-type organic thermoelectrics: demonstration of *ZT* > 0.3. *Nat. Commun.* **11**, 5694 (2020).

Acknowledgements We acknowledge the financial support from the National Natural Science Foundation of China (T2425010 (T.L.), 52303216 (K.L.), 52403219 (Z.Z.), 52373010 (J.H.), and T2441002 (Y.G.)), the Beijing Natural Science Foundation (JQ22006 (T.L.)), the Strategic Priority Research Program of the Chinese Academy of Sciences (XDB0520000 (Y.G. and C.D.)) and the CAS Project for Young Scientists in Basic Research (YSBR-053 (Y.G.)). K.L. appreciates the Boya Postdoctoral Fellowship of Peking University. We acknowledge the Molecular Materials and Nanofabrication Laboratory, the Materials Processing and Analysis Center and the Electron Microscopy Laboratory of Peking University for instrument use. The computational part is supported by the High-Performance Computing Platform of Peking University. We thank beamline BL14B1 (Shanghai Synchrotron Radiation Facility) for providing beamtime for part of the X-ray scattering measurement. We also acknowledge technical support of mechanical property measurements from the State Key Laboratory of Advanced Optical Polymer and Manufacturing Technology.

Author contributions T.L. conceived the idea and supervised the project. K.L., J.W. and T.L. designed the experiments. X.P., J.C. and C.W. synthesized the conjugated polymers and crosslinker. K.L. explored the bulk nanophase separation and the thermally activable crosslinking. K.L. and J.W. performed the selection of n-type dopants and the generality of the TEE design strategy. J.W. fabricated the elastic TEG and conducted the performance testing. S.-Y.T. and X.-Y.D. performed the atomistic molecular dynamics simulation. K.L. and Yudong Liu conducted the mechanical property characterizations. K.L. and P.L. did the GIWAXS measurement. Y.D., D.W. and C.D. conducted the thermal conductivity measurements. C.-K.P. and J.P. synthesized the thermally activatable n-dopant TAM. F.Q., J.L. and J.H. supplied the insulating elastomers and performed the mechanical tests. Y.G. and Yunqi Liu provided the AFM, UV–vis absorption and surface energy measurements and helped with the data analysis. K.L., J.W., Z.Z. and T.L. wrote the paper. All authors discussed and revised the paper.

Competing interests K.L., J.W. and T.L. have filed a patent application on this work (202510116577.7). The other authors declare no competing interests.

Additional information

Supplementary information The online version contains supplementary material available at https://doi.org/10.1038/s41586-025-09387-z.

Correspondence and requests for materials should be addressed to Ting Lei.

Peer review information *Nature* thanks Francisco Molina-Lopez and the other, anonymous, reviewer(s) for their contribution to the peer review of this work. Peer reviewer reports are available.

Reprints and permissions information is available at http://www.nature.com/reprints.

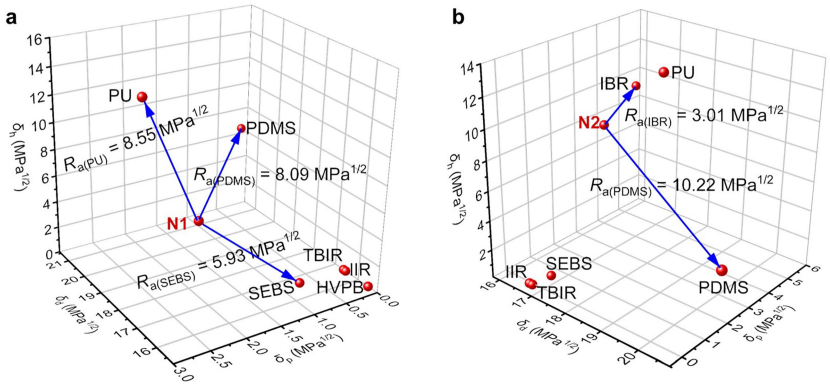

Extended Data Fig. 1 | Hansen solubility parameters (HSPs) of the thermoelectric polymers (a, N1 and b, N2) and elastomers. HSP consists of three parameters representing different interactions, including δ_d for dispersion (van der Waals interactions), δ_p for polarity (dipole moment interactions), and δ_h for hydrogen bonding. The solubility distance (R_a) between the conjugated polymer and elastomer is determined by the formula: $(R_a)^2 = 4(\delta_{d2}-\delta_{d1})^2 + (\delta_{p2}-\delta_{p1})^2 + (\delta_{h2}-\delta_{h1})^2$. Lower R_a implies better miscibility between two materials. The HSPs and R_a of the thermoelectric polymers and elastomers are summarized in Supplementary Table 2.

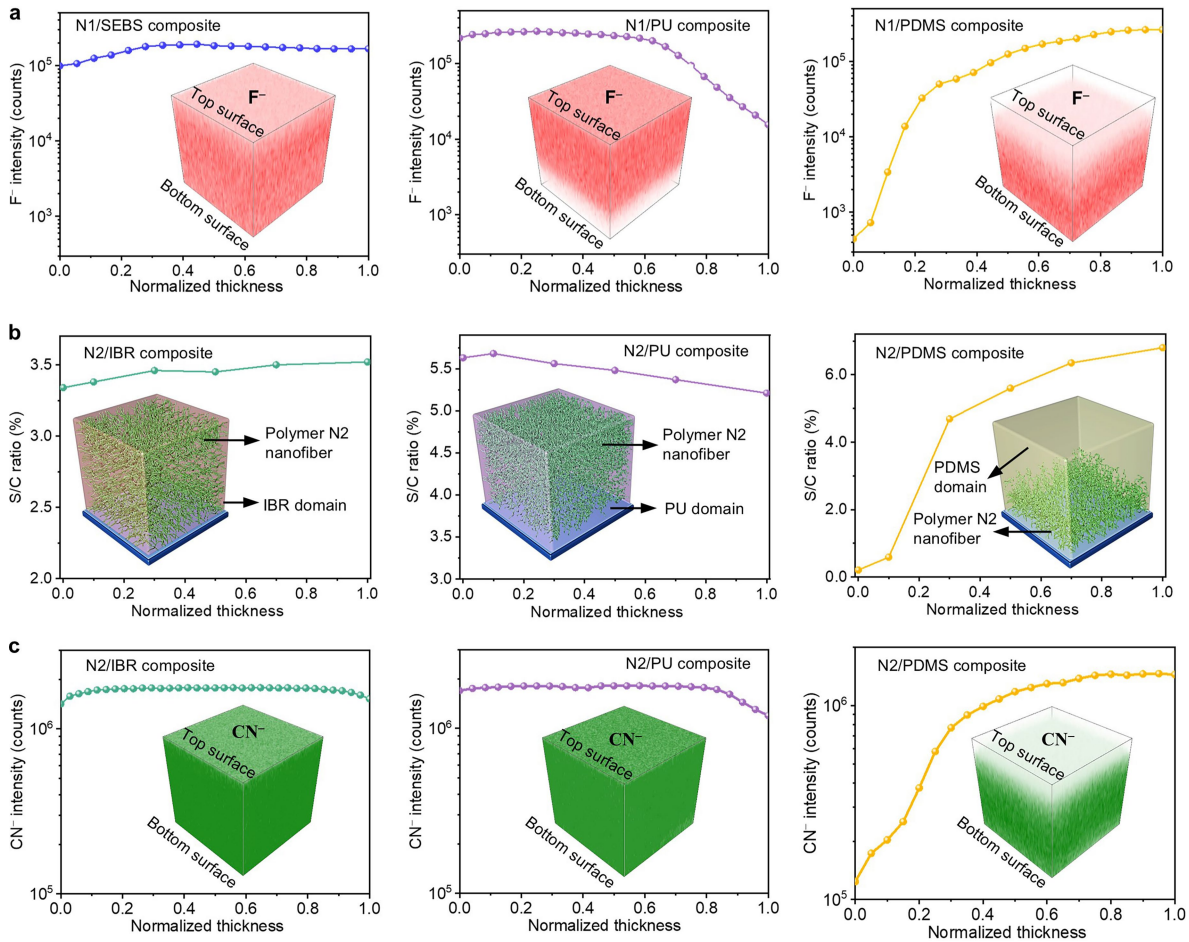

Extended Data Fig. 2 | Vertical phase separation analysis of the polymer/elastomer blending system. a, ToF-SIMS depth profiles of the characteristic F^- ion for polymer N1 in composite films. Inset, the corresponding 3D illustration of F^- ions in the composite film as a function of film depth. **b**, Ratio changes between S(2p) and C(1 s) peak (S/C ratio) obtained from the XPS profile element analysis of the N2/elastomer composites. Inset, the corresponding 3D illustration of the vertical phase separation. **c**, ToF-SIMS depth profiles of the characteristic CN^- ion for polymer N2 in composite films. Inset, the corresponding 3D illustration of CN^- ions in the composite film as a function of film depth.

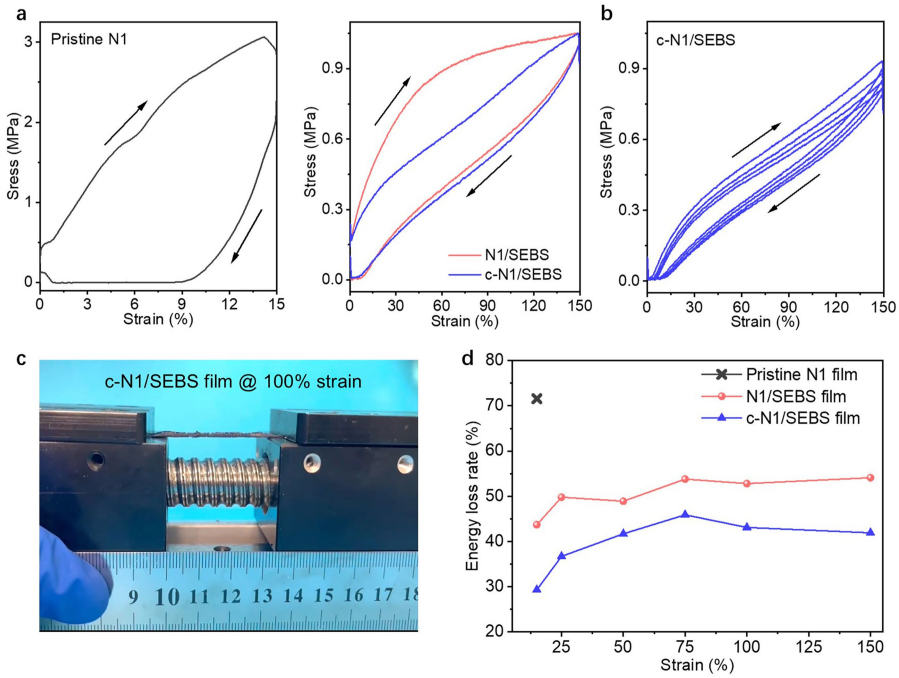

Extended Data Fig. 3 | Uniform bulk nanophase separation and thermally activable crosslinking to enhance elastic resilience. a, The first stretching-releasing cycles of the pristine N1, N1/SEBS and c-N1/SEBS (5 wt% crosslinker). **b**, The second to fifth stretching-releasing cycles of c-N1/SEBS. **c**, Photograph of a freestanding c-N1/SEBS film on a stretching station. **d**, Energy loss rate of the first stretching-releasing cycle for pristine N1, N1/SEBS, and c-N1/SEBS films under different strains ranging from 15% to 150%.